water

MDPI

Article

Photocatalytic Dye Degradation and Bio-Insights of Honey-Produced α-Fe_2O_3 Nanoparticles

Mohamed Sharmila [1,*], Ramasamy Jothi Mani [2], Chelliah Parvathiraja [3], Sheik Mohammed Abdul Kader [4], Masoom Raza Siddiqui [5], Saikh Mohammad Wabaidur [5], Md Ataul Islam [6] and Wen-Cheng Lai [7,8,*]

1 Research Scholar (18211192132009), Department of Physics, Sadakathullah Appa College, Tirunelveli-627011 Affiliated to Manonmaniam Sundarnar University, Tirunelveli 627012, Tamilnadu, India
2 Assistant Professor, Department of Physics, Fatima College, Madurai 625018, Tamilnadu, India; drjothifatima@gmail.com
3 Department of Physics, Manonmaniam Sundaranar University, Tirunelveli 627012, Tamilnadu, India; cpraja1206@gmail.com
4 Department of Physics, Sadakathullah Appa College, Tirunelveli 627011, India; smabdulkader@sadakath.ac.in
5 Chemistry Department, College of Science, King Saud University, Riyadh 11451, Saudi Arabia; siddiqui124@gmail.com (M.R.S.); swabaidur@ksu.edu.sa (S.M.W.)
6 Division of Pharmacy and Optometry, School of Health Sciences, Faculty of Biology, Medicine and Health, University of Manchester, Manchester M13 9PL, UK; ataul.islam80@gmail.com
7 Bachelor Program in Industrial Projects, National Yunlin University of Science and Technology, Douliu 640301, Taiwan
8 Department of Electronic Engineering, National Yunlin University of Science and Technology, Douliu 640301, Taiwan
* Correspondence: msharmilaphysics@sadakath.ac.in (M.S.); wenlai@yuntech.edu.tw or wenlai@mail.ntust.edu.tw (W.-C.L.)

Abstract: Iron oxide nanoparticles are produced using simple auto combustion methods with honey as a metal-stabilizing and -reducing agent. Herein, α-Fe_2O_3 nanoparticles are produced using an iron nitrate precursor. These prepared samples are analyzed by an X-ray diffractometer (XRD), FTIR spectroscopy, UV-DRS, and a field-emission scanning electron microscope (FESEM) combined with energy-dispersive spectroscopy and a vibrating sample magnetometer (VSM). The XRD results confirm a rhombohedral structure with an $R3\bar{c}$ space group single-phase formation of α-Fe_2O_3 in all samples. FESEM images reveal the different morphologies for the entire three samples. TEM analysis exhibits spherical shapes and their distribution on the surfaces. XPS spectroscopy confirms the Fe-2p and O-1s state and their valency. The VSM study shows strong ferromagnetic behavior. The prepared α-Fe_2O_3 nanoparticles exhibit exceptional charge carriers and radical production. The prepared sample retains excellent photocatalytic, antifungal and antibacterial activity.

Keywords: hematite; structural properties; magnetic properties

Citation: Sharmila, M.; Mani, R.J.; Parvathiraja, C.; Kader, S.M.A.; Siddiqui, M.R.; Wabaidur, S.M.; Islam, M.A.; Lai, W.-C. Photocatalytic Dye Degradation and Bio-Insights of Honey-Produced α-Fe_2O_3 Nanoparticles. *Water* **2022**, *14*, 2301. https://doi.org/10.3390/w14152301

Academic Editors: Mika Sillanpää and Peyman Gholami

Received: 24 June 2022
Accepted: 17 July 2022
Published: 24 July 2022

1. Introduction

Through the incremental extension of novel technologies and inventions, many industries have utilized modern compounds for their manufacturing units. Dyes have become an unavoidable ingredient in the paint, toys, and textile industries. Untreated sewage from industrial wastewater contains uncoated dye materials, remaining dyes, and undissolved inorganic salts. The presence of a high amount of dye components in wastewater may be harmful to terrain, and have a negative impact on marine creatures and microbes present in the aquatic ecosystem [1]. The treatment of wastewater is necessary for the survival of human and aquatic living beings. Eliminating these kinds of dyes has become an interesting field of study and exploration. A dye given great attention is methylene blue (MB) dye, which is a bluish dye in its oxidation condition. Due to its high-quality antifungal properties, MB is applied in the medical field. The excessive use of MB dye in food stuff and

medicine can create nausea, gastrointestinal disorder, etc. To completely remove it from water bodies, different established methods such as ultrafiltration, ion exchange, biological treatment, chlorination, oxidation, anaerobic degradation, reverse osmosis, flocculation, adsorption, coagulation, photocatalytic degradation, and ozonation [2–4] are used, along with several metals, metal oxide, conducting polymers and zeolites. Among them, metal oxides play a very important role in many areas of chemistry, physics, and materials science. Metal oxides (MOs) play a key role in the areas of material science, sensors, UV shielding, photovoltaics, hydrogen generation, dye degradation, anti-fogging glass, photocatalysts, adsorption [5–12], etc. In recent years, plentiful approaches have been projected for the synthesis of metal oxide, including methods such as microemulsion, auto combustion, co-precipitation, the sol–gel method, the non-aqueous route, pyrolysis reaction, thermal decomposition, solvothermal, hydrothermal, and mechano-chemical processing, emulsion techniques, laser ablation, gamma ray irradiation, solid-state reaction, and sono-chemical preparation [13–17]. Additionally, with some of these methods, toxic chemicals are used in the fusion, which produces non-eco-friendly, unsafe and hazardous byproducts. Removal is a laborious process and, therefore, there is a huge demand for the use of green methods in the production of nanoparticles. Green chemistry synthesis has drawn market attention as it is humble, low cost, and environmentally friendly. Some commonly known MOs, including TiO_2, ZnO, Fe_2O_3, SnO_2, VO, CuO, Co_3O_4, MoO, etc., are used in photocatalytic application. Photocatalytic dye degradation is one of the best degradation methods to remove pollutants from the environment. Additionally, methylene blue (MB) dye has many disadvantages, including toxic and carcinogenic effects and skin irritation [6–17]. Among these MOs, Fe_2O_3 has been given much attention due to its high efficiency and easy recovery. Iron oxide nanoparticles exist in varied polymorphs such as magnetite (Fe_3O_4), maghemite (ν-Fe_2O_3), hematite (α-Fe_2O_3), and goethite (Fe-OOH). Hematite is a stable candidate in both chemical and thermodynamic conditions. Hematite nanoparticles have considerable application in the fields of catalysis, sensing, data loading, dye stuffs, degradation agents, water waste management, photochemical cells, solar cells, hydrogen production, and cosmetics [18–21]. With the assistance of a reducing and stabilizing agent, one can effectively obtain densely packed magnetic nanoparticles and control their size and shape. Recently, biosynthesis methods have received attention due to their eco-friendly and simplistic processes, economic feasibility, low waste generation, and therapeutic application. For the good yield and purity of a sample, three criteria should be followed: (i) selecting a solvent; (ii) using a reducing agent; and (iii) using non-hazardous material as a capping agent. For the past few years, honey-directed green synthesis has been applied for the synthesis of gold, silver, carbon, platinum, and palladium nanoparticles. The monosaccharides, carbohydrates, enzymes, vitamins, minerals, antioxidant proteins, amino acids and vitamin C in honey, which also contains a poly hydroxyl group, could help in reducing and stabilizing nanoparticles. Alkaline pH honey can convert silver ions into Ag NPs [22]. Chromium oxide nanoparticles can be rapidly synthesized by the reduction of potassium dichromate solution using natural honey [23]. Similarly, $CoFe_2O_4$, $ZnFe_2O_4$, $NiFe_2O_4$ and $Ag/CoFe_2O_4$ have been synthesized using natural honey as an oxidizing precursor [23–26]. To the best of our understanding, this is the first work regarding the effects of different precursors on the synthesis of hematite α-Fe_2O_3 nanoparticles using honey as a reducing agent with the analysis of structural and magnetic properties. An auto combustion method set for an easy procedure to produce α-Fe_2O_3 nanoparticles is used in the present investigation. The α-Fe_2O_3 nanoparticles are characterized for their structural, morphological and optical properties by various characterization techniques such as X-ray diffraction (XRD), field effective scanning electron microscopy (FESEM), Fourier transform infra-red (FT-IR) spectroscopy, diffuse reflection spectroscopic (DRS) analysis, and vibrating sample magnetometry (VSM). Antibacterial and antifungal activity are examined against standard pathogens.

2. Materials and Methods

2.1. Materials

The following chemicals were used for the present investigation without any further purification: iron nitrate [$Fe(NO_3)_3 \cdot 9H_2O$,97%, Himedia-Mumbai-India], Honey (Marthandam, Tamil Nadu, India).

2.2. Synthesis Method

First, 0.3 M $Fe(NO_3)_3 \cdot 9H_2O$ was dissolved in 50 mL of DM water. For gelation purposes, 2 mL of honey was added in an iron solution. Honey acts as reducing and stabilization agent in the process. The honey-loaded solution was stirred separately and heated at a temperature of 60 °C under constant magnetic stirring (REMI 1MLH), until the solution color turned from a transparent yellow solution to a brick red color indicating the iron nitrate solution. Then, the resultant brick red solution was dehydrated in a hot air oven at 120 °C for 12 h to obtain a powder. After that, the product was grounded using an agate mortar and pestle. Then, the dried samples were annealed in an INDFURR furnace at 600 °C for 2 h. The obtained brownish red color powder was stored and kept at room temperature for further characterization studies. The prepared sample was denoted as an FNH code.

2.3. Characterizations

The prepared FNH sample was characterized by X-ray diffractometer analysis with XPERT-PRO by Cu kα monochromatic radiation (kα = 1.5406 Å), operated at 40 kV and 30 mA at a 2 h angle pattern. The structural building block of the hematite phase was extracted from the powder diffraction pattern. The scanning was carried out in the region from 20 to 80 with a 0.02 step rate. The surface consistency and elemental composition of the synthesized samples were identified with TEM (Titan, Bangalore, India) and a field scanning electron microscope (FESEM) equipped with an energy-dispersive X-ray (EDX) (SUPRA55 CARL ZEISS, Aalen, Germany). The material valency and binding energy were measured by XPS spectroscopy (XPS-PHI 5000, Chanhassen, MN, USA). The magnetic behavior of the FNH sample was measured with a vibrating sample magnetometer (Lakeshore VSM 7410, Westerville, OH, USA) at room temperature for the application of the field from −15 to +15 kOe.

2.4. Antimicrobial Activity

The disc dispersion method was used to scrutinize the antimicrobial movement of the synthesized FNH nanoparticles. Gram (+) bacteria such as *S. aureus* (ATCC 6538) and *B. subtilis* (ATCC 6633) and Gram (−) bacteria such as *E. coli* (ATCC 8739) and *Pseudomonas aerosinosa* (ATCC 27853) were utilized to determine the antimicrobial activity of the FNH nanoparticles. Similarly, to identify antifungal action, the well diffusion technique was implemented against three fungi, namely, *Pendicium* (11597), *Aspergillus niger* (16404), and *A. Flavus* (9643)). A cork borer was used to dig 5 mm wells in the medium. To evaluate the nearly 20 µL (20 µg) of Muller–Hinton agar and PDA medium, and 50 µL of (α-Fe_2O_3) nanoparticles loaded to each plate to calculate the activity, the zone of inhibition was measured after 24 h The zone formation gave the results of the antimicrobial and antifungal activity of the FNH nanoparticles.

2.5. Photocatalytic Activity

The photocatalytic degradation of MB dye using simulated solar radiation. To carry out the reaction, initially, 50 mL of MB (1×10^{-5} mole and pH = 6.15) was taken in a 250 mL beaker. The distance between the simulated light and the beaker was almost 10 cm. About 0.05 g of photo catalyst was added to the solution and kept in the dark for 2 hrs to reach the adsorption and desorption kinetics. After 2 h, the solution was placed in simulated solar radiation with continuous stirring at an RPM of 550. Then, the solution was withdrawn

at 10 min intervals, centrifuged, and the rate of the degradation of the dye was measured using a spectrophotometer of MB.

The % degradation of the dye was determined using the following formula:

$$\text{Percentage of dye degradation} = C_{MBi} - C_{MBT} / C_{Mbi} \times 100$$

where:

C_{MBi} = initial dye concentration;

C_{MBT} = concentration of dye solution at time interval t hours of simulated solar irradiation.

3. Result and Discussion

3.1. XRD Analysis

The X-ray diffraction (XRD) pattern of the prepared FNH nanoparticles using iron nitrate precursors is depicted in Figure 1 All the obtained diffraction peaks of hematite α-Fe_2O_3 matched well with the JCPDS file number 85-0599 [27]. This indicates the formation of single-phase hematite α-Fe_2O_3 nanoparticles. The average crystallite size of the samples was determined using Scherer's formula, and was found to be around 32 to 42 nm. The lattice parameters of all the samples were well matched with the published report [27].

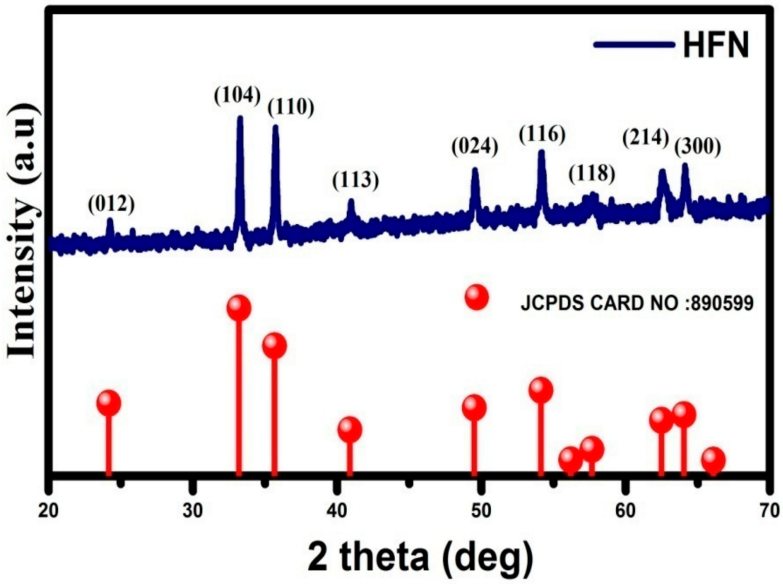

Figure 1. X-RD pattern of synthesized FNH nanoparticles.

3.2. FESEM Analysis

The typical FESEM images and qualitative elemental composition (EDX spectra) of FNH samples are depicted in Figure 2. The effect of changing the surface morphology of the α-Fe_2O_3 nanoparticles prepared using hexose sugar (honey) can clearly be seen. In the FESEM image, the particle size is more or less spherical in shape with no uniformity in morphology. This proves the precursor was acting as a stabilizer for particles via the selective deceleration of growth rate, preventing the agglomeration of the particles. The α-Fe_2O_3 nanoparticles demonstrated the existence of honey on the surface, provoking agglomeration and inducing particle formation. The hexose sugar reduced the nitrate and formed the α-Fe_2O_3 nanoparticles, which can be observed from the FESEM images. The elemental peak of iron and the oxygen peaks only were presented in the EDX spectrum. No other peaks could be noticed; this suggests that pure α-Fe_2O_3 nanoparticles were attained. The EDX spectrum confirmed the existence of nanophase iron oxide and the XRD results. The obtained results show the effects of the precursor on the creation of dissimilar phases of iron oxide nanoparticles, and are well matched with the previous reported iron oxide nanoparticles [28].

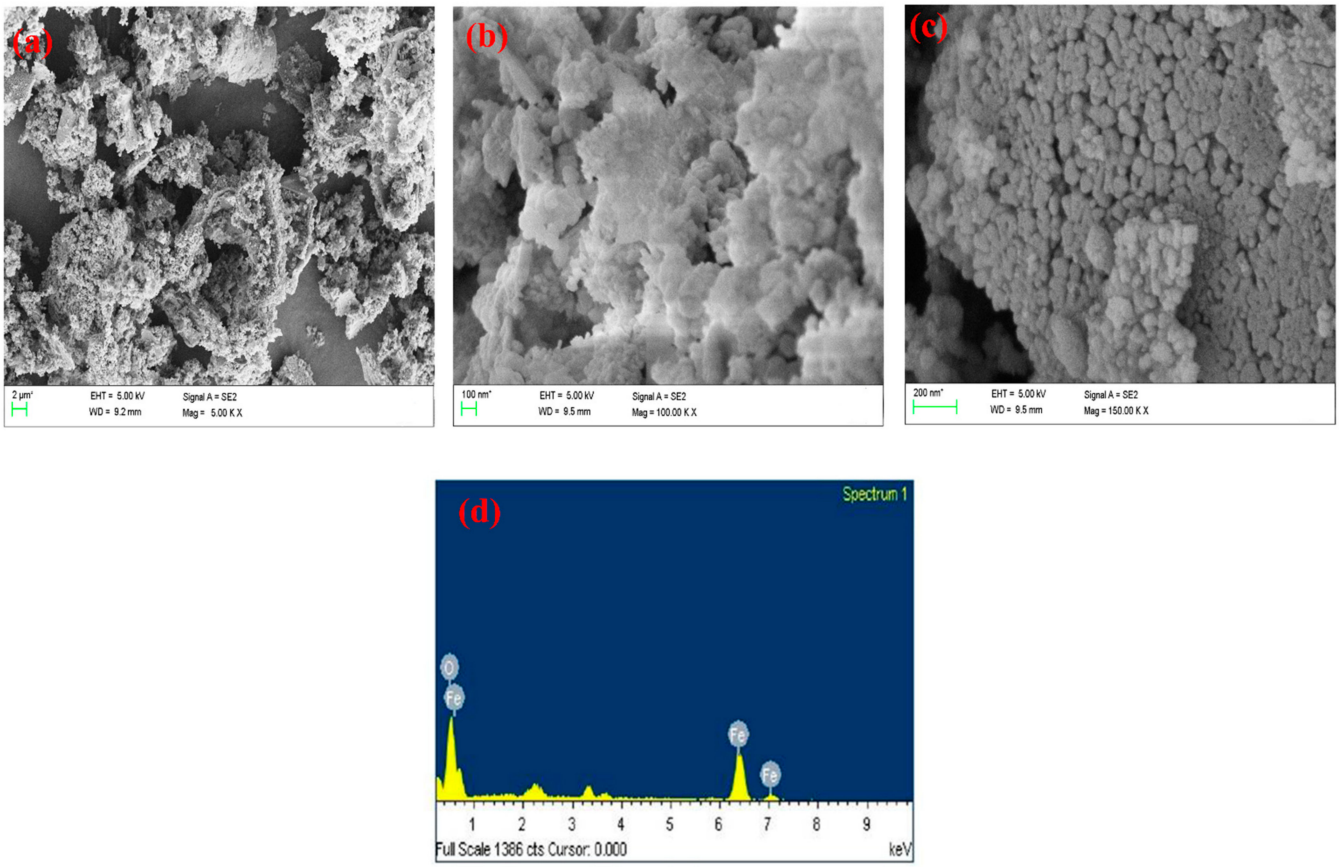

Figure 2. (**a**–**c**) FESEM image of prepared FNH nanoparticles at lower and higher magnifications and (**d**) EDAX spectrum of FNH nanoparticles.

3.3. VSM Analysis

The magnetization curve for hematite nanoparticles is shown in Figure 3 with the M-H curve of the FNH nanoparticles. The observed values of retentivity (M_r), coercivity (H_C), and the saturated magnetization (M_S) of the FNH samples are listed in Table 1, along with the earlier available results in the literature, which observed a decrease in Fe-Fe interatomic bond distance and the volume of the unit cells. The magnetic phenomenon can be explained in terms of mean field theory; according to this theory, the distance between two magnetic ions, if larger than their sum of ionic radii, interacts ferromagnetically as the distance reduces between these ions, their ferromagnetic interaction is suppressed, and antiferromagnetic interactions are enacted [29–34]. The values of the bond lengths between Fe-O, O-O, and Fe-Fe are shown in Table 1, showing that the formation of iron oxide is ferromagnetic in nature compared with previous iron oxide magnetic insights.

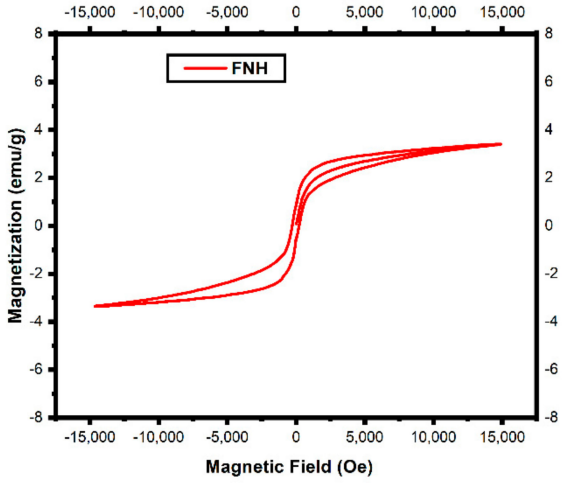

Figure 3. VSM spectrum of FNH nanoparticles.

Table 1. Magnetic parameters of FNH sample.

Precursors	Synthesized Method	Temperature	M_S emu/g	H_C Oe	M_r emu/g	Reference
$FeCl_3$	Green	60 °C/2 h	10.01	200	1.03	[29]
$FeCl_3 \cdot 6H_2O$	Green	60 °C/2 h	8.5			[30]
$Fe(C_5H_7O_2)_3$	Chemical	400 °C/6 h	0.41			[31]
$FeCl_3$	Chemical	300 °C/1 h	66.6	SPM		[32]
$FeCl_3$	Chemical	600 °C/3 h	0.3152	771.52	0.0369	[33]
$FeNO_3$	Chemical	500 °C/5 h	1.7	200		[34]
$Fe(NO_3)_3 \cdot 9H_2O$	Green	600 °C/2 h	0.8448	501.18	0.25531	Present Work

3.4. FTIR Analysis

The formation of chemical bonds in the samples was confirmed using FTIR spectroscopy. Figure 4 reveals the FTIR spectra of the prepared FNH sample. The results show forcible absorption bonds around 553 and 431 cm^{-1} with slightly different magnitudes. These bands represent characteristic features of hematite and correspond to metal oxide stretching vibrations. The high-frequency band at around 553 cm^{-1} refers to Fe-O deformation in the octahedral site, and Fe-O deformation in tetrahedral site is revealed from the frequency band at around 433 cm^{-1} [35]. At last, the 1098 cm^{-1} band present in the FNH sample corresponds to the presence of C-O bond stretching in the C-O-C group in the anhydro glucose ring due to glucose content [36].

3.5. PL Analysis

The photoluminescence of the prepared α-Fe_2O_3 nanoparticle is shown in Figure 5. The intense and sharp emission band around 590 nm indicates the edge emission and corresponds to the optical absorption. The enhanced neighboring Fe^{3+} magnetic coupling is due to the change in the atomic oxygen coordinates in the nanosized α-Fe_2O_3 lattice [37]. This is also due to the increase in Fe–O bonding separation, which is also responsible for photoluminescence. The PL peaks around 590 nm may also be due to the surface defects which may arise from the deep traps created due to iron vacancies. The PL spectrum of α-Fe_2O_3 exhibits a broad band centered at 590 nm that shifts to a slightly higher energy compared to the previously reported α-Fe_2O_3. As a result, the PL spectrum of the synthesized α-Fe_2O_3 nanoparticle shows no recombination mechanism.

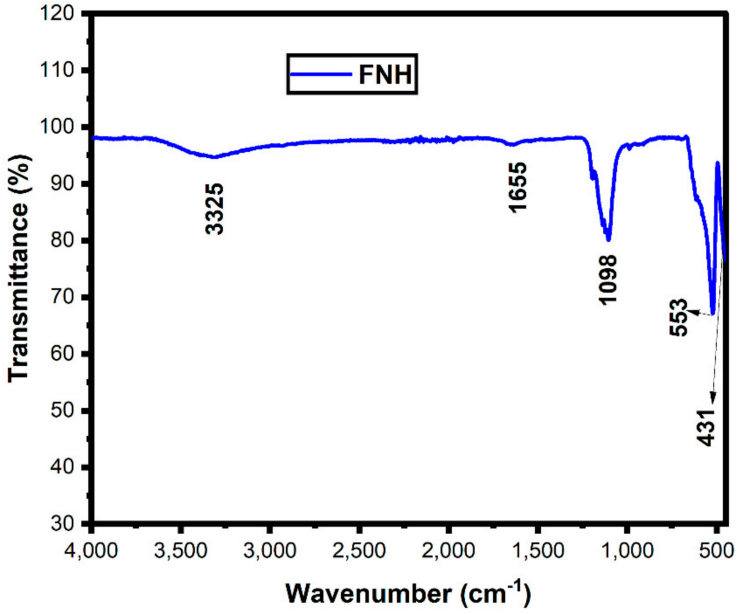

Figure 4. FTIR spectrum of FNH nanoparticle.

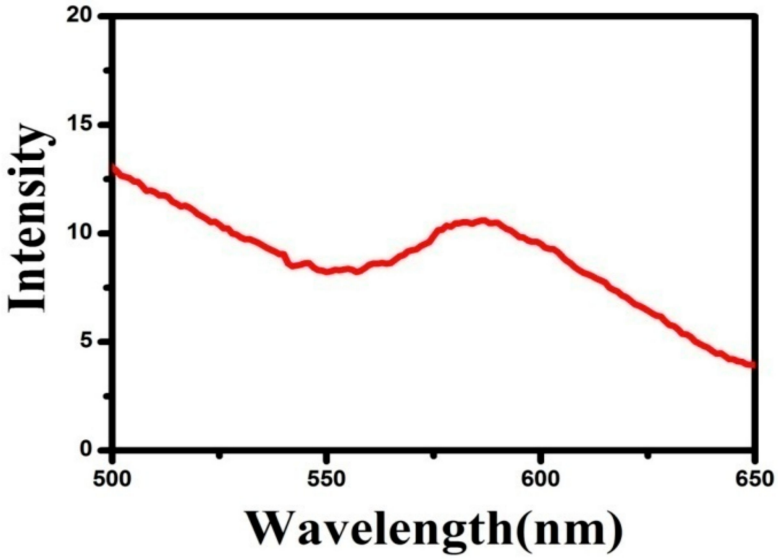

Figure 5. PL spectrum of FNH nanoparticles.

3.6. UV DRS Analysis

The honey-mediated synthesis of the α-Fe_2O_3 nanoparticles' optical absorbance and bandgap spectrum is visualized in Figure 6a,b. The iron oxide absorbance regions reside at around 600 nm in the visible region. The visible region absorption enhanced the photo charge carrier generation, and visible light absorption was adequate to degrade the bacterial and toxic wastages [22–26].

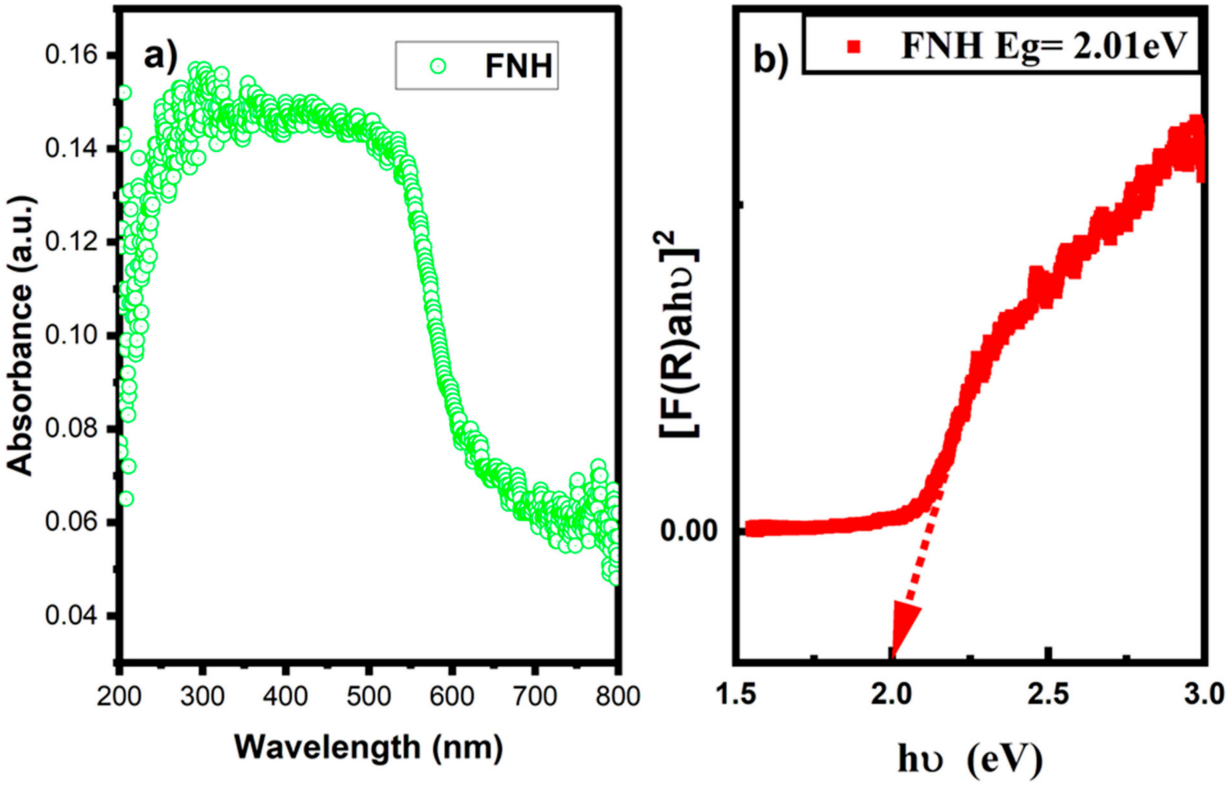

Figure 6. (**a**) UV absorbance and (**b**) Tauc plot of FNH nanoparticles.

The optical band gap energy (*Eg*) of the prepared sample can be estimated by the Tauc equation:

$$(\alpha h\nu)\mathrm{n} = \mathrm{A}(h\nu - Eg)^2$$

where A is a constant that is determined by the valence and conduction bands of particular materials; $h\nu$ is the photon energy; α is the absorption coefficient; and n is 2 for an indirect transition.

Figure 6 shows the $(\alpha h\nu)2 \sim h\nu$ curves of the prepared samples. The bandgap energies of FNH at 2.01 eV, which were close to the literature values for the indirect bandgap of α-Fe_2O_3 [37–41], are compared in Table 2. The narrow bandgap energy shows the formation of iron oxide nanoparticles and their optical imperfections.

Table 2. UV-DRS bandgap comparisons with XRD and FTIR of α-Fe_2O_3 nanoparticles.

S. No	D (nm)	FTIR Metal Oxide Bond (cm^{-1})		Band Gap *Eg* (eV)	Reference
1	38	527	434	2.13	[38]
2	37.6	545	480	2.53	[39]
3	33	525	433	2.01	**Present work**

3.7. TEM Analysis

The green synthesized α-Fe_2O_3 (FNH) nanoparticles' transmission electron microscopic images are displayed in Figure 7a,b. Various magnifications are presented in FNH nanoparticles and their magnifications are 50 nm and 100 nm. Figure 7a demonstrates the accumulation of spherical particles on the surface. The aggregation and accumulation of a large number of particles result from the honey biomolecules [42]. The existing honey molecules create the agglomerations on the surface and form the accumulation for the

derived shapes. The spherical FNH samples are evident in Figure 7b. The spherical shape of the nanoparticles reveals the improved photocatalytic degradation activity and bacterial deactivations [43,44]. The spherical-shaped FNH nanoparticles are at a size of around 31 nm. The obtained particle size values are nearly equal to the crystallite size of the FNH nanoparticles.

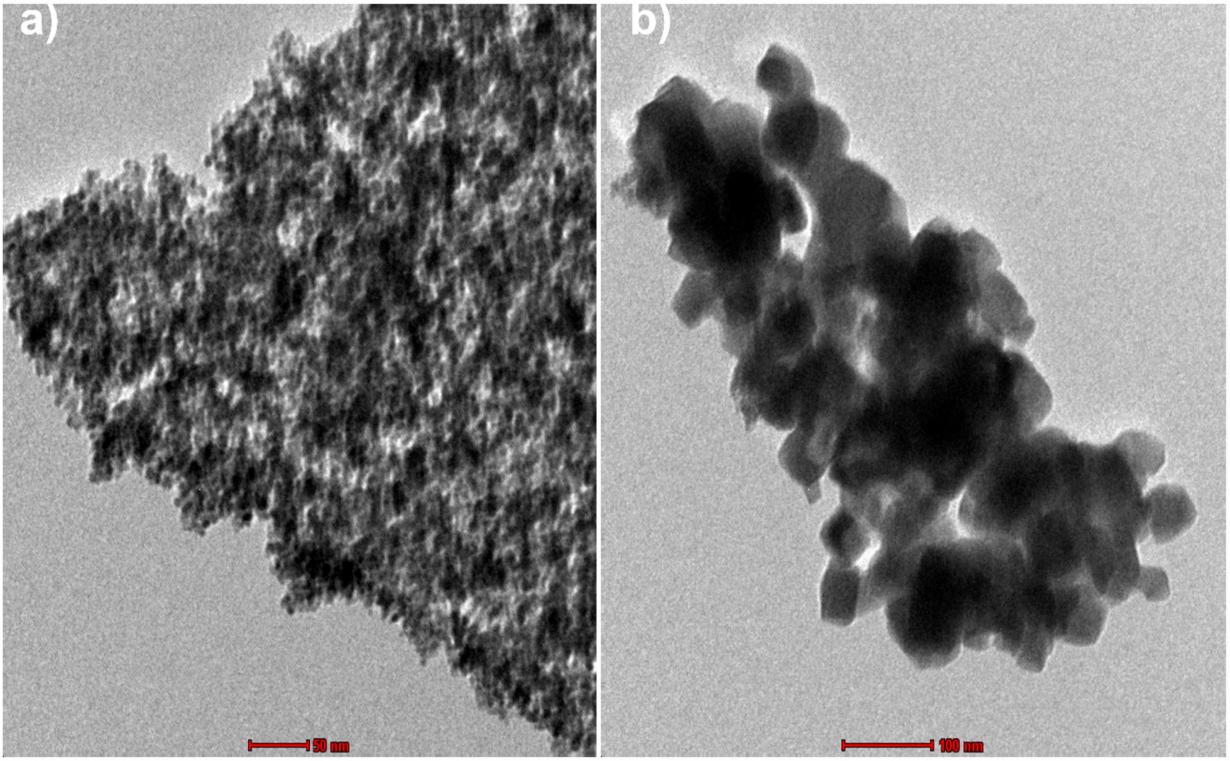

Figure 7. (**a**,**b**) TEM images of synthesized FNH nanoparticles.

3.8. XPS Analysis

The XPS spectrum aids in determining the valency and bonding between the materials and binding the energy of the synthesized nanoparticles. Figure 8 presents the XPS wide, Fe-2p, O-1s and C-1s spectrum of the FNH nanoparticles. The wide spectrum of the FNH samples derives from the elements of Fe, O and C from the synthesized FNH nanoparticles (Figure 8a). The Fe-2p spectrum denotes the valency of the Fe elements in the 2p state and their binding energies are 711.4 eV (Fe-2$p_{3/2}$) and 724.5 eV (Fe-2$p_{1/2}$). Fe^{2+} and Fe^{3+} were stabilized from the honey bio-derivatives. The honey compounds reduced the iron to zero valency [45]. The oxygen attachment on the Fe increased the surface area and reduced electron trapping. Lattice oxygen peaks were present at 531, and 15 eV represents the O-1s state which formed the Fe-O bonding and confirmed the FN nanoparticles of α-Fe_2O_3 [46]. The carbon peak for the FNH nanoparticles was obtained from the 284.75 eV and 288.97 eV binding energies, representing C-O and C=O at the O-1s state. Carbon attribution on the FNH nanoparticles confirms the honey molecules' interaction with the Fe and O elements [47–49]. The obtained XPS results show the Fe and O elements and their bonding and reduction/stabilization confirmation from the honey molecules.

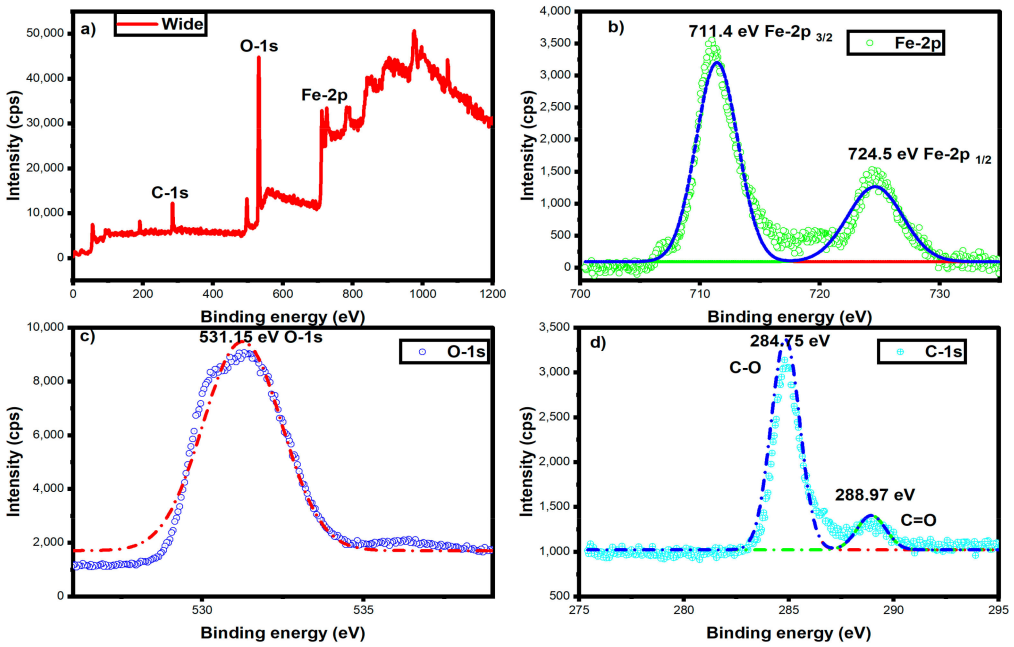

Figure 8. XPS (**a**) wide, (**b**) Fe-2p, (**c**) O-1s, and (**d**) C-1s spectrum of FNH nanoparticles.

3.9. Photocatalytic Studies

The photocatalytic dye degradation of α-Fe_2O_3 nanoparticles prepared using honey is depicted in Figure 9. Simulated solar radiation acts as the energy source of photo degradation. The light source modifies the valence band energy and conduction band energy in the dye-mediated α-Fe_2O_3 nanoparticles. The excited electrons are separated by source materials during the excitation process. Simultaneously, the same amount of holes are captured by the valence band. The α-Fe_2O_3 nanoparticles exhibited strong degradation at the initial 30 min. The light addition to the catalyst and dye solution resulted in photogenerated charge carriers [50]. The photogenerated charge carriers produced the enhanced photocatalytic activity towards the MB dye solution. At 120 min, the MB dye degraded to 76 percent of the α–Fe_2O_3 nanoparticles synthesized using honey. The degradation efficiency, as shown in Figure 10, indicates the possible mechanism of α-Fe_2O_3 nanoparticles in MB dye degradation, and their values compared with previous work are displayed in Table 3. Initially, the light irradiation to the α-Fe_2O_3 nanoparticles produces the electron-hole pairs. Then, the electrons are occupied by the conduction band and holes are occupied by the valence band. The holes and electrons produce $O^{2-}$and $OH^{\cdot}$ radicals for the mineralization of the organic molecules [51,52]. These super oxides and hydroxyl are responsible for the degradation of the methylene blue dye. The degradation mechanism is shown in Figure 11, and its equation is as follows.

$$(\alpha\text{-}Fe_2O_3) + h\nu \rightarrow (\alpha\text{-}Fe_2O_3)V.B^{h+} + (\alpha\text{-}Fe_2O_3)C.B^{(e-)} \quad (1)$$

$$(\alpha\text{-}Fe_2O_3)V.B^{(h+)} + H_2O \rightarrow (\alpha\text{-}Fe_2O_3) + H^+ + OH^- \quad (2)$$

$$(\alpha\text{-}Fe_2O_3)C.B^{(e-)} + OH^- \rightarrow (\alpha\text{-}Fe_2O_3) + OH \quad (3)$$

$$(\alpha\text{-}Fe_2O_3)^{h+} + O_2 \rightarrow {}^{\cdot}O_2 \quad (4)$$

$$O_2{}^- + OH/h^+ + Dye^+ \rightarrow \text{Mineralized products} \quad (5)$$

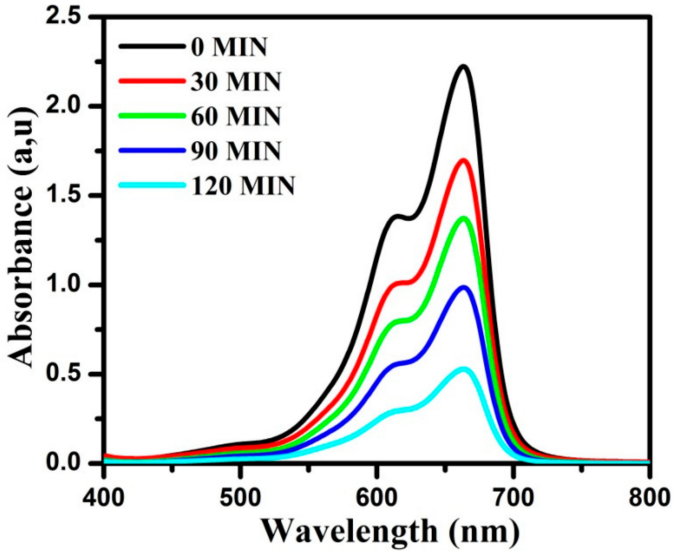

Figure 9. Photocatalytic degradation spectrum of FNH nanoparticles.

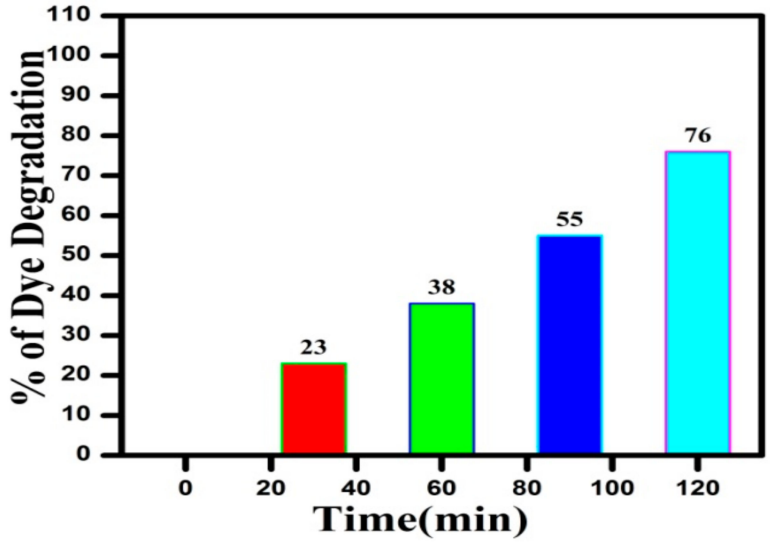

Figure 10. Percentage of degradation of FNH nanoparticles of MB dye vs. time.

Table 3. α-Fe_2O_3 nanoparticles compared with other metal/metal oxide nanoparticles.

Si No	Compound Name	Dye Source	Degradation Efficiency	Dye Volume	Catalytic Load	Reference
1	CuO-SWCNT	MB	97.33%/2 h	100 mL	150 mg	[52]
2	CuO	MB	78%/120 min	50 mL (10 ppm)	50 mg	[53]
3	Co_3O_4	MB	86%/45 min	20 mL 50 mg/L	5 mg	[54]
4	NiO NPs	MB	65.5%/180 min	20 mL	10 mg	[55]
5	ZnO	MB	97.5%/30 min	20mL	0.5mg	[56]
6	ZnO NPs	MB	98%/90 min	50 mL (10 µM)	5–15 mg	[57]
7	rGO/TiO_2/ ZnO	MB	92%/120 min	100 mL (0.3 mg/L)	0.1 g/L	[58]

Table 3. *Cont.*

Si No	Compound Name	Dye Source	Degradation Efficiency	Dye Volume	Catalytic Load	Reference
8	Ag doped TiO_2)	MB	82.3%/2 h	100 mL (7000 mg/L)	1.0 g	[59]
9	MgO	MB	64%/150 min	25.0 mL	10.0 mg	[60]
10	Vanadium-doped MgO nanoparticles	MB	92%/120 min	400 mL (10 ppm)	50 mg (125 mg/L)	[61]

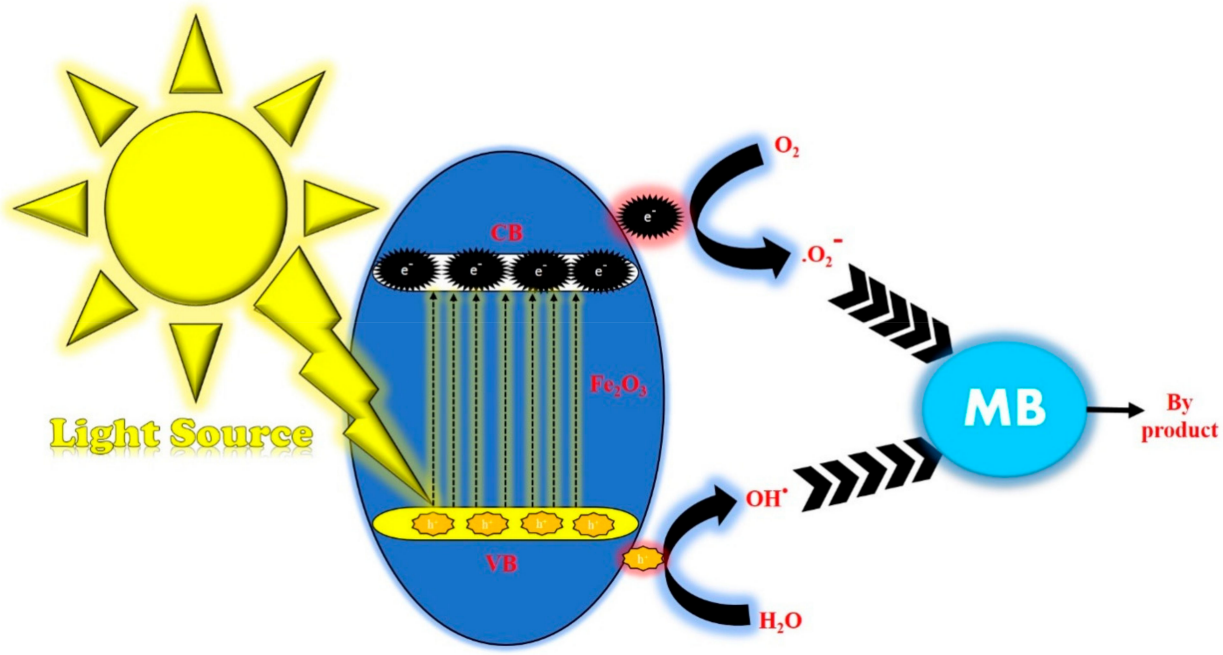

Figure 11. Photocatalytic degradation mechanism of FNH nanoparticles.

3.10. Antimicrobial and Antifungal Activity

The synthesized FNH nanoparticles were evaluated for antibacterial and antifungal activity using the well diffusion method for *Staphylococcus aureus*, *Bacillus subtilis*, *Escherichia coli*, *Pseudomonas aeruginosa*, *Pencillium*, *Aspergillus niger,* and *A. flavus*. The observations and their values are presented in Figure 12 and tabulated in Table 4. The results displayed for (+) bacteria were more active than the results for (−) bacteria in the FNH nanoparticles. The FNH nanoparticles were more stable, so their release of ions into the environment was minimal compared with the other metal oxides. In the activity, the UV light promoted the reactive oxygen species in the electron-hole pair recombination process in the α-Fe_2O_3 nanoparticles. In both cases, the process led to the formation of Fe^{3+} ions, superoxide (O_2^-), hydroxyl radicals (-OH), singlet oxygen ($^1O_2$), and hydrogen peroxide (H_2O_2) [61,62]. These formed free radicals were destroyed by cell membranes because of their electrostatic interactions between the nanoparticles and the bacteria. The reason behind the mechanism is the size and surface of the α-Fe_2O_3 nanoparticles. Hence, iron has a powerful reducing agent which enhances DNA damage, ROS production, and cell membrane disorder. In addition, the results suggest the biocidal potential of α-Fe_2O_3 nanoparticles.

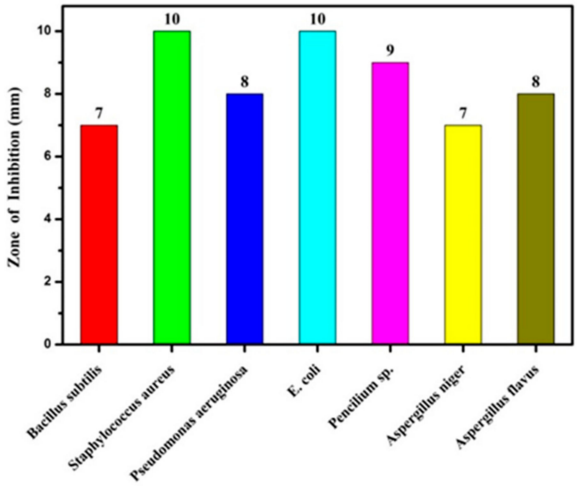

Figure 12. Zones of inhibited FNH for bacteria and fungi.

Table 4. Biological activity of α-Fe2O3 nanoparticles.

Zone of Inhibition (mm)						
Bacillus subtilis	***Staphylococcus aureus***	***Pseudomonas aeruginosa***	***E. coli***	***Pencilium* sp.**	***Aspergillus niger***	***Aspergillus flavus***
7	10	8	10	9	7	8

4. Conclusions

In this article, hematite (α-Fe_2O_3) nanoparticles were synthesized by an auto combustion method. This method leads to a rapid reaction process and obtains average crystallites ranging between 30 and 45 nm in size. The effect of nitrate precursors on size and magnetic behavior was studied. The honey solution played a vital role in the sample structural parameters, morphology, and magnetic possessions of the sample. The FNH sample exhibited high magnetization with low coercivity, which may be correlated with bond length. Furthermore, it is significant that the green method of honey used in this study also has a strong influence on the shape, size and morphology of hematite nanoparticles. The valency of Fe and O, their charge carrier production, and their electron mitigations were analyzed by XPS analysis. Moreover, the honey molecules' incorporation of hematite (α-Fe_2O_3) nanoparticles controlled the e-h pair recombination and increased the visible light absorption. Their inclusion increased the reactive oxygen species and radical activity. Based on the obtained findings, hematite (α-Fe_2O_3) nanoparticles could be vital players in drug development and organic pollutant removal applications.

Author Contributions: Conceptualization, M.S. and R.J.M.; methodology, R.J.M.; software, C.P.; validation, S.M.A.K., R.J.M. and M.S.; formal analysis, M.S.; investigation, R.J.M.; resources, S.M.W., M.R.S., M.A.I. and W.-C.L.; data curation, C.P.; writing—original draft preparation, M.S.; writing—review and editing, M.S.; visualization, M.S.; supervision, R.J.M.; project administration, R.J.M.; funding acquisition, S.M.W. All authors have read and agreed to the published version of the manuscript.

Funding: The authors are grateful to the Researchers Supporting Project No. (RSP-2021/326), King Saud University, Riyadh, Saudi Arabia.

Institutional Review Board Statement: Not applicable.

Informed Consent Statement: Not applicable.

Data Availability Statement: All research data used to assist the findings of this work are included within the manuscript.

Acknowledgments: The authors thank the management of Sadakathullah Appa College, Tiru-nelveli, Tamilnadu India for providing opportunity to carry out this research. Manonmaniam Sundaranar University, Tirunelveli, Tamilnadu, India. Authors are grateful to the Researchers Supporting Project No. (RSP-2021/326), King Saud University, Riyadh, Saudi Arabia.

Conflicts of Interest: The authors declare no conflict of interest.

References

1. Mehra, S.; Singh, M.; Chadha, P. Adverse impact of textile dyes on the aquatic environment as well as on human beings. *Toxicol. Int.* **2021**, *28*, 165–176.
2. Bose, S.; Tripathy, B.K.; Debnath, A.; Kumar, M. Boosted sono-oxidative catalytic degradation of Brilliant green dye by magnetic $MgFe_2O_4$ catalyst: Degradation mechanism, assessment of bio-toxicity and cost analysis. *Ultrason. Sonochem.* **2021**, *75*, 105592. [CrossRef] [PubMed]
3. Rafiq, A.; Ikram, M.; Ali, S.; Niaz, F.; Khan, M.; Khan, Q.; Maqbool, M. Photocatalytic degradation of dyes using semiconductor photocatalysts to clean industrial water pollution. *J. Ind. Eng. Chem.* **2021**, *97*, 111–128. [CrossRef]
4. Issaka, E.; Amu-Darko, J.N.O.; Yakubu, S.; Fapohunda, F.O.; Ali, N.; Bilal, M. Advanced catalytic ozonation for degradation of pharmaceutical pollutants—A review. *Chemosphere* **2022**, *289*, 133208. [CrossRef]
5. Gupta, S.K.; Mao, Y. A review on molten salt synthesis of metal oxide nanomaterials: Status, opportunity, and challenge. *Prog. Mater. Sci.* **2021**, *117*, 100734. [CrossRef]
6. Manjakkal, L.; Szwagierczak, D.; Dahiya, R. Metal oxides based electrochemical pH sensors: Current progress and future perspectives. *Prog. Mater. Sci.* **2020**, *109*, 100635. [CrossRef]
7. Lizundia, E.; Armentano, I.; Luzi, F.; Bertoglio, F.; Restivo, E.; Visai, L.; Torre, L.; Puglia, D. Synergic effect of nanolignin and metal oxide nanoparticles into Poly (l-lactide) bionanocomposites: Material properties, antioxidant activity, and antibacterial performance. *ACS Appl. Bio. Mater.* **2020**, *3*, 5263–5274. [CrossRef]
8. Zhou, K.L.; Wang, Z.; Han, C.B.; Ke, X.; Wang, C.; Jin, Y.; Zhang, Q.; Liu, J.; Wang, H.; Yan, H. Platinum single-atom catalyst coupled with transition metal/metal oxide heterostructure for accelerating alkaline hydrogen evolution reaction. *Nat. Commun.* **2021**, *12*, 3783. [CrossRef]
9. Gautam, S.; Agrawal, H.; Thakur, M.; Akbari, A.; Sharda, H.; Kaur, R.; Amini, M. Metal oxides and metal organic frameworks for the photocatalytic degradation: A review. *J. Environ. Chem. Eng.* **2020**, *8*, 103726. [CrossRef]
10. Park, C.; Kim, T.; Kim, Y.I.; Lee, M.W.; An, S.; Yoon, S.S. Supersonically sprayed transparent flexible multifunctional composites for self-cleaning, anti-icing, anti-fogging, and anti-bacterial applications. *Compos. Part B Eng.* **2021**, *222*, 109070. [CrossRef]
11. Fatima, R.; Warsi, M.F.; Zulfiqar, S.; Ragab, S.A.; Shakir, I.; Sarwar, M.I. Nanocrystalline transition metal oxides and their composites with reduced graphene oxide and carbon nanotubes for photocatalytic applications. *Ceram. Int.* **2020**, *46*, 16480–16492. [CrossRef]
12. Dehghani, F.; Ayatollahi, S.; Bahadorikhalili, S.; Esmaeilpour, M. Synthesis and characterization of mixed–metal oxide nanoparticles ($CeNiO_3$, $CeZrO_4$, $CeCaO_3$) and application in adsorption and catalytic oxidation–decomposition of asphaltenes with different chemical structures. *Pet. Chem.* **2020**, *60*, 731–743. [CrossRef]
13. Dheyab, M.A.; Aziz, A.A.; Jameel, M.S.; Noqta, O.A.; Mehrdel, B. Synthesis and coating methods of biocompatible iron oxide/gold nanoparticle and nanocomposite for biomedical applications. *Chin. J. Phys.* **2020**, *64*, 305–325. [CrossRef]
14. Han, D.; Zhao, M. Facile and simple synthesis of novel iron oxide foam and used as acetone gas sensor with sub-ppm level. *J. Alloy. Compd.* **2020**, *815*, 152406. [CrossRef]
15. Gahrouei, Z.E.; Imani, M.; Soltani, M.; Shafyei, A. Synthesis of iron oxide nanoparticles for hyperthermia application: Effect of ultrasonic irradiation assisted co-precipitation route. *Adv. Nat. Sci. Nanosci. Nanotechnol.* **2020**, *11*, 025001. [CrossRef]
16. Imran, M.; Riaz, S.; Shah, S.M.H.; Batool, T.; Khan, H.N.; Sabri, A.N.; Naseem, S. In-vitro hemolytic activity and free radical scavenging by sol-gel synthesized Fe_3O_4 stabilized ZrO_2 nanoparticles. *Arab. J. Chem.* **2020**, *13*, 7598–7608. [CrossRef]
17. Belles, L.; Moularas, C.; Smykała, S.; Deligiannakis, Y. Flame spray pyrolysis Co_3O_4/CoO as highly-efficient nanocatalyst for oxygen reduction reaction. *Nanomaterials* **2021**, *11*, 925. [CrossRef]
18. Garcia-Osorio, D.; Hidalgo-Falla, P.; Peres, H.E.; Gonçalves, J.M.; Araki, K.; Garcia-Segura, S.; Picasso, G. Silver enhances hematite nanoparticles-based ethanol sensor response and selectivity at room temperature. *Sensors* **2021**, *21*, 440. [CrossRef]
19. Frindy, S.; Sillanpää, M. Synthesis and application of novel α-Fe_2O_3/graphene for visible-light enhanced photocatalytic degradation of RhB. *Mater. Des.* **2020**, *188*, 108461. [CrossRef]
20. Najaf, Z.; Nguyen, D.L.T.; Chae, S.Y.; Joo, O.S.; Shah, A.U.H.A.; Vo, D.V.N.; Nguyen, V.H.; Van Le, Q.; Rahman, G. Recent trends in development of hematite (α-Fe_2O_3) as an efficient photoanode for enhancement of photoelectrochemical hydrogen production by solar water splitting. *Int. J. Hydrogen Energy* **2021**, *46*, 23334–23357. [CrossRef]
21. Mazloum-Ardakani, M.; Sadri, N.; Eslami, V. Detection of dexamethasone sodium phosphate in blood plasma: Application of hematite in electrochemical sensors. *Electroanalysis* **2020**, *32*, 1148–1154. [CrossRef]
22. Al-Zaban, M.I.; Mohamed, A.M.; Maha, A.A. Catalytic degradation of methylene blue using silver nanoparticles synthesized by honey. *Saudi J. Biol. Sci.* **2021**, *28*, 2007–2013. [CrossRef]

23. Nivethitha, P.R.; Rachel, D.C.J. A study of antioxidant and antibacterial activity using honey mediated Chromium oxide nanoparticles and its characterization. *Mater. Today Proc.* **2020**, *48*, 276–281. [CrossRef]
24. Gingasu, D.; Mindru, I.; Culita, D.C.; Calderon-Moreno, J.M.; Bartha, C.; Greculeasa, S.; Iacob, N.; Preda, S.; Oprea, O. Structural, morphological and magnetic investigations on cobalt ferrite nanoparticles obtained through green synthesis routes. *Appl. Phys. A* **2021**, *127*, 892. [CrossRef]
25. Inbaraj, D.J.; Chandran, B.; Mangalaraj, C. Synthesis of $CoFe_2O_4$ and $CoFe_2O_4$/g-C_3N_4 nanocomposite via honey mediated sol-gel auto combustion method and hydrothermal method with enhanced photocatalytic and efficient Pb^{+2} adsorption property. *Mater. Res. Express* **2019**, *6*, 055501. [CrossRef]
26. Yadav, R.S.; Kuřitka, I.; Vilcakova, J.; Havlica, J.; Masilko, J.; Kalina, L.; Tkacz, J.; Enev, V.; Hajdúchová, M. Structural, magnetic, dielectric, and electrical properties of $NiFe_2O_4$ spinel ferrite nanoparticles prepared by honey-mediated sol-gel combustion. *J. Phys. Chem. Solids* **2017**, *107*, 150–161. [CrossRef]
27. GarcíaMartínez, T.; López, J.M.; Solsona, B.; Sanchis, R.; Willock, D.J.; Davies, T.E.; Lu, L.; He, Q.; Kiely, C.J.; Taylor, S.H. The key role of nanocasting in gold-based Fe_2O_3 nanocasted catalysts for oxygen activation at the metal-support interface. *ChemCatChem* **2019**, *11*, 1915–1927.
28. Kumar, D.; Singh, H.; Jouen, S.; Hannoyer, B.; Banerjee, S. Effect of precursor on the formation of different phases of iron oxide nanoparticles. *RSC Adv.* **2015**, *5*, 7138–7150. [CrossRef]
29. Basavegowda, N.; Mishra, K.; Lee, Y.R. Synthesis, characterization, and catalytic applications of hematite (α-Fe_2O_3) nanoparticles as reusable nanocatalyst. *Adv. Nat. Sci. Nanosci. Nanotechnol.* **2017**, *8*, 025017. [CrossRef]
30. Karade, V.C.; Parit, S.B.; Dawkar, V.V.; Devan, R.S.; Choudhary, R.J.; Kedge, V.V.; Pawarh, N.V.; Kim, J.H.; Chougale, A.D. A green Approach for the Synthesis of α-Fe_2O_3 Nanoparticles from Gardenia Resinifera Plant and It's In vitro hyperthermia application. *Heilyon* **2019**, *5*, e02044. [CrossRef]
31. Islam, M.S.; Kurawaki, J.; Kusumoto, Y.; Abdulla-Al-Mamun, M.; Mukhlish, M.B. Hydrothermal novel synthesis of neck-structured hyperthermia-suitable magnetic (Fe_3O_4 2019, γ-Fe_2O_3 and α-Fe_2O_3) nanoparticles. *J. Sci. Res.* **2012**, *4*, 99–107. [CrossRef]
32. Dehsari, H.S.; Ribeiro, A.H.; Ersöz, B.; Tremel, W.; Jakob, G.; Asadi, K. Effect of precursor concentration on size evolution of iron oxide nanoparticles. *CrystEngComm* **2017**, *19*, 6694–6702. [CrossRef]
33. Rufus, A.; Sreeju, N.; Philip, D. Synthesis of biogenic hematite (α-Fe_2O_3) nanoparticles for antibacterial and nanofluid applications. *RSC Adv.* **2016**, *6*, 94206–94217. [CrossRef]
34. Arora, A.K.; Sharma, M.; Kumari, R.; Jaswal, V.S.; Kumar, P. Synthesis, characterization, and magnetic studies of-nanoparticles. *J. Nanotechnol.* **2014**, *2014*, 474909. [CrossRef]
35. Si, J.-C.; Xing, Y.; Peng, M.L.; Zhang, C.; Buske, N.; Chen, C.; Cui, Y.L. Solvothermal synthesis of tunable iron oxide nanorods and their transfer from organic phase to water phase. *CrystEngComm* **2014**, *16*, 512–516. [CrossRef]
36. Rosliza, R.; Nik, W.W.; Izman, S.; Prawoto, Y. Anti-corrosive properties of natural honey on Al–Mg–Si alloy in seawater. *Curr. Appl. Phys.* **2010**, *10*, 923–929. [CrossRef]
37. Bouhjar, F.; Ullah, S.; Chourou, M.L.; Mollar, M.; Marí, B.; Bessaïs, B. Electrochemical fabrication and characterization of p-CuSCN/n-Fe2O3 heterojunction devices for hydrogen production. *J. Electrochem. Soc.* **2017**, *164*, H936. [CrossRef]
38. Lassoued, A.; Lassoued, M.S.; Dkhil, B.; Ammar, S.; Gadri, A. Synthesis, structural, morphological, optical and magnetic characterization of iron oxide (α-Fe_2O_3) nanoparticles by precipitation method: Effect of varying the nature of precursor. *Phys. E: Low-Dimens. Syst. Nanostruct.* **2018**, *97*, 328–334. [CrossRef]
39. Bashir, A.K.H.; Furqan, C.M.; Bharuth-Ram, K.; Kaviyarasu, K.; Tchokonté, M.B.T.; Maaza, M. Structural, optical and Mössbauer investigation on the biosynthesized α-Fe_2O_3: Study on different precursors. *Phys. E Low-Dimens. Syst. Nanostruct.* **2019**, *111*, 152–157. [CrossRef]
40. Dehno Khalaji, A. Spherical α Fe_2O_3 Nanoparticles: Synthesis and Characterization and Its Photocatalytic Degradation of Methyl Orange and Methylene Blue. *Phys. Chem. Res.* **2022**, *10*, 473–483.
41. Liu, T.; Zhang, S.; Wang, Z.; Xu, Y. Preparation and characterization of α-Fe_2O_3/Fe_3O_4 heteroplasmon nanoparticles via the hydrolysis-combustion-calcination process of iron nitrate. *Mater. Res. Express* **2022**, *9*, 045011. [CrossRef]
42. Kushwaha, P.; Chauhan, P. Influence of different surfactants on morphological, structural, optical, and magnetic properties of α-Fe_2O_3 nanoparticles synthesized via co-precipitation method. *Appl. Phys. A* **2022**, *128*, 18. [CrossRef]
43. Vijayakumar, T.; Benoy, M.; Duraimurugan, J.; Kumar, G.S.; Shkir, M.; Maadeswaran, P.; Srinivasan, R.; Prabhu, S.; Ramesh, R.; Haseena, S. Investigation on photocatalytic activity of g-C_3N_4 decorated α-Fe_2O_3 nanostructure synthesized by hydrothermal method for the visible-light assisted degradation of organic pollutant. *Diam. Relat. Mater.* **2022**, *125*, 109021. [CrossRef]
44. Fatimah, I.; Purwiandono, G.; Hidayat, A.; Sagadevan, S.; Kamari, A. Mechanistic insight into the adsorption and photocatalytic activity of a magnetically separable γ-Fe_2O_3/Montmorillonite nanocomposite for rhodamine B removal. *Chem. Phys. Lett.* **2022**, *792*, 139410. [CrossRef]
45. Zhang, W.; Guan, H.; Kuang, C.; Wang, W.; Hu, Y.; Yang, X. Boosting charge transfer for α-Fe_2O_3 semiconductor with the coupling of chiral monolayer. *Mater. Lett.* **2022**, *308*, 131130. [CrossRef]
46. Nguyen, T.B.; Dinh Thi, T.H.; Pham Minh, D.; Bui Minh, H.; Nguyen Thi, N.Q.; Nguyen Dinh, B. Photoreduction of CO_2 to CH_4 over Efficient Z-Scheme-Fe_2O_3/g-C_3N_4 Composites. *J. Anal. Methods Chem.* **2022**, *2022*, 1358437. [CrossRef] [PubMed]

47. Zhang, Y.; Wang, Q.; Zhu, K.; Ye, K.; Wang, G.; Cao, D.; Yan, J. Edge sites-driven accelerated kinetics in ultrafine Fe_2O_3 nanocrystals anchored graphene for enhanced alkali metal ion storage. *Chem. Eng. J.* **2022**, *428*, 131204. [CrossRef]
48. Güneş, F.; Aykaç, A.; Erol, M.; Erdem, Ç.; Hano, H.; Uzunbayir, B.; Şen, M.; Erdem, A. ¸Synthesis of hierarchical hetero-composite of graphene foam/α-Fe_2O_3 nanowires and its application on glucose biosensors. *J. Alloy. Compd.* **2022**, *895*, 162688. [CrossRef]
49. Bai, J.; Shen, R.; Chen, W.; Xie, J.; Zhang, P.; Jiang, Z.; Li, X. Enhanced photocatalytic H2 evolution based on a $Ti_3C_2/Zn_{0.7}Cd_{0.3}S/Fe_2O_3$ Ohmic/S-scheme hybrid heterojunction with cascade 2D coupling interfaces. *Chem. Eng. J.* **2022**, *429*, 132587. [CrossRef]
50. Barbero, N.; Vione, D. Why does should not be used to test the photocatalytic activity of semiconductor oxides. *Environ. Sci. Technol.* **2016**, *50*, 2130. [CrossRef]
51. Sapkota, K.P.; Lee, I.; Hanif, M.A.; Islam, M.A.; Akter, J.; Hahn, J.R. Enhanced visible-light photocatalysis of nanocomposites of copper oxide and single-walled carbon nanotubes for the degradation of methylene blue. *Catalysts* **2020**, *10*, 297.
52. Sorekine, G.; Anduwan, G.; Waimbo, M.N.; Osora, H.; Velusamy, S.; Kim, S.; Kim, Y.S.; Charles, J. Photocatalytic studies of copper oxide nanostructures for the degradation of methylene blue under visible light. *J. Mol. Struct.* **2022**, *1248*, 131487. [CrossRef]
53. Dhiman, S.; Gupta, B. Co_3O_4 nanoparticles synthesized from waste Li-ion batteries as photocatalyst for degradation of methyl blue dye. *Environ. Technol. Innov.* **2021**, *23*, 101765. [CrossRef]
54. Miri, A.; Mahabbati, F.; Najafidoust, A.; Miri, M.J.; Sarani, M. Nickel oxide nanoparticles: Biosynthesized, characterization and photocatalytic application in degradation of methylene blue dye. *Inorg. Nano-Met. Chem.* **2022**, *52*, 122–131. [CrossRef]
55. Lu, J.; Batjikh, I.; Hurh, J.; Han, Y.; Ali, H.; Mathiyalagan, R.; Ling, C.; Ahn, J.C.; Yang, D.C. Photocatalytic degradation of methylene blue using biosynthesized zinc oxide nanoparticles from bark extract of Kalopanaxseptemlobus. *Optik* **2019**, *182*, 980–985. [CrossRef]
56. Narath, S.; Koroth, S.K.; Shankar, S.S.; George, B.; Mutta, V.; Wacławek, S.; Černík, M.; Padil, V.V.T.; Varma, R.S. Cinnamomumtamala leaf extract stabilized zinc oxide nanoparticles: A promising photocatalyst for methylene blue degradation. *Nanomaterials* **2021**, *11*, 1558. [CrossRef]
57. Raghavan, N.; Thangavel, S.; Venugopal, G. Enhanced photocatalytic degradation of methylene blue by reduced graphene-oxide/titanium dioxide/zinc oxide ternary nanocomposites. *Mater. Sci. Semicond. Process.* **2015**, *30*, 321–329. [CrossRef]
58. Whang, T.-J.; Huang, H.Y.; Hsieh, M.T.; Chen, J.J. Laser-induced silver nanoparticles on titanium oxide for photocatalytic degradation of methylene blue. *Int. J. Mol. Sci.* **2009**, *10*, 4707–4718. [CrossRef]
59. Sackey, J.; Bashir, A.K.H.; Ameh, A.E.; Nkosi, M.; Kaonga, C.; Maaza, M. Date pits extracts assisted synthesis of magnesium oxides nanoparticles and its application towards the photocatalytic degradation of methylene blue. *J. King Saud Univ.-Sci.* **2020**, *32*, 2767–2776. [CrossRef]
60. Patil, H.R.; Murthy, Z.V.P. Vanadium-doped magnesium oxide nanoparticles formation in presence of ionic liquids and their use in photocatalytic degradation of methylene blue. *Acta Metall. Sin. Engl. Lett.* **2016**, *29*, 253–264. [CrossRef]
61. He, W.; Kim, H.K.; Wamer, W.G.; Melka, D.; Callahan, J.H.; Yin, J.J. Photogenerated charge carriers and reactive oxygen species in ZnO/Au hybrid nanostructures with enhanced photocatalytic and antibacterial activity. *J. Am. Chem. Soc.* **2014**, *136*, 750–757. [CrossRef]
62. Maezono, T.; Tokumura, M.; Sekine, M.; Kawaswe, Y. Hydroxyl radical concentration profile in photo-Fenton oxidation process: Generation and consumption of hydroxyl radicals during the discoloration of azo-dye Orange II. *Chemosphere* **2011**, *82*, 1422–1430. [CrossRef]